Novel ZVS S-TCM Modulation of Three-Phase AC/DC Converters

M. Haider, J. Azurza, S. Mirić, N. Nain, G. Zulauf, J. W. Kolar
Power Electronic Systems Laboratory (PES)
ETH Zurich, Switzerland
haider@lem.ee.ethz.ch

D. Xu
Zhejiang University
Zhejiang, China

G. Deboy
Infineon Tech. Austria AG
Villach, Austria

Abstract—For three-phase AC-DC power conversion, the widely-used continuous current mode (CCM) modulation scheme results in relatively high semiconductor losses from hard-switching each device during half of the mains cycle. Triangular current mode (TCM) modulation, where the inductor current reverses polarity before turn-off, achieves zero-voltage-switching (ZVS) but at the expense of a wide switching frequency variation (15× for the three-phase design considered here), complicating filter design and compliance with EMI regulations. In this paper, we propose a new modulation scheme, sinusoidal triangular current mode (S-TCM), that achieves soft-switching, keeps the maximum switching frequency below the $150\,\mathrm{kHz}$ EMI regulatory band, and limits the switching frequency variation to only 3×. Under S-TCM, three specific modulation schemes are analyzed, and a loss-optimized weighting of the current bands across load is identified. The $2.2\,\mathrm{kW}$ S-TCM phase-leg hardware demonstrator achieves $99.7\,\%$ semiconductor efficiency, with the semiconductor losses accurately analytically estimated within $10\,\%$ $(0.3\,\mathrm{W})$. Relative to a CCM design, the required filter inductance is $6\times$ lower, the inductor volume is $37\,\%$ smaller, and the semiconductor losses are $55\,\%$ smaller for a simultaneous improvement in power density and efficiency.

I. INTRODUCTION

AC-DC power conversion underpins modern electrical infrastructure, serving as the key conversion stage for ubiquitous and critical applications. For three-phase (3-Φ) converters, in particular, use cases include photovoltaic (PV) inverters to connect solar arrays to the grid and power-factor-correction (PFC) rectifiers, among many others with application-specific demands on cost, power density, and efficiency. For the modular kW-scale bridge legs considered here (see **Table I**), applications include on-board electric vehicle chargers (e.g. for Level 2 charging at $6.6\,\mathrm{kW}$), data center power supplies (typically built with modularity for use cases in the $6.6\,\mathrm{kW}$ to $10\,\mathrm{kW}$ range), and aircraft motor drives (with power levels as low as $750\,\mathrm{W}$ even in 3-Φ systems).

To achieve average sinusoidal currents on the AC side of these power converters, a standard half-bridge leg with an output filter (see **Fig. 1(a)**) is typically used. In grid-tied rectifiers and inverters, these sinusoidal average phase currents (i.e. $i_\mathrm{a}(t) = \hat{i}\sin(\omega_\mathrm{ac}t)$) are controlled to be in phase with the phase voltages that are shown in **Fig. 1(b)**, and the output filter is required to meet harmonics and emissions regulations (e.g. [1]–[4]). Output filters for motor drives, similarly, reduce radiated emissions from the inverter-motor cables, eliminate $\mathrm{d}v/\mathrm{d}t$-related motor winding insulator stress, and limit bearing currents from common-mode voltage excitations.

The passive components – especially the inductor – of the filter stage dominate the size and weight of these power converters [5,6]. To minimize the required inductance and

shrink the filter inductor, the switching frequency of the bridge-leg can be increased at the expense of higher switching losses and lower efficiency. This tension recalls the familiar power electronics trade-off between power density and efficiency [7]. For the specific case of AC-DC converters, then, an implementation with both low-inductance requirements *and* high-efficiency is sought.

Three-phase rectifier and inverter systems in the kW power range considered here (see **Table I**) are typically operated in continuous current mode (CCM) [8], where the current is controlled to a low-ripple envelope around the sinusoidal average output current i_a. This low-ripple envelope leads to low current stress, but the bridge-leg transistors are each hard-switched for half of the mains cycle. These hard-switching losses limit the switching frequency to around $20\,\mathrm{kHz}$ to $50\,\mathrm{kHz}$, say, for systems with $U_\mathrm{dc} = 800\,\mathrm{V}$ (to interface with the European $400\,\mathrm{V}$ line-to-line mains) and $1200\,\mathrm{V}$ SiC MOSFETs, resulting in a high AC-side inductance and therefore a large inductor.

To eliminate these hard-switching losses and enable higher switching frequencies, modulation schemes and architectures with zero-voltage-switching (ZVS) of the power devices across the line cycle have been proposed [9,10]. Triangular current mode (TCM) modulation, a well-known approach (for example, in single-phase rectifiers [11] and motor drives [12]) that is shown in **Fig. 1(c.i)**, achieves ZVS with the basic half-bridge converter structure and without additional auxiliary circuits. Numerous other schemes for introducing ZVS have been proposed – including the use of auxiliary circuitry [13], an unfolder-based TCM scheme for single-phase rectifiers [14], a T-type-architecture circuit for TCM [15,16], complex current control approaches based on boundary conduction mode (BCM) or critical conduction mode (CRM) [17]–[19], and a decoupled model for simplified control [20] – but TCM is still considered the state-of-the-art and is the most widely-used commercially.

The approaches based on BCM and CRM have been described for an open-star point of the first filter stage, leading to a coupling of the phases that complicates the control. This additional degree-of-freedom can be utilized to achieve a nearly-constant switching frequency, which is beneficial for EMI, and/or to facilitate the separation of the differential (DM) and common-mode (CM) filter stages. Separating the DM and CM filter stages, however, is not necessarily beneficial for power density and/or efficiency [21], and here we use the filter approach of **Fig. 1(a)** [11], where the phases are decoupled and 3-Φ common-mode (CM) inductors are avoided. This implementation, then, allows the individual control of each
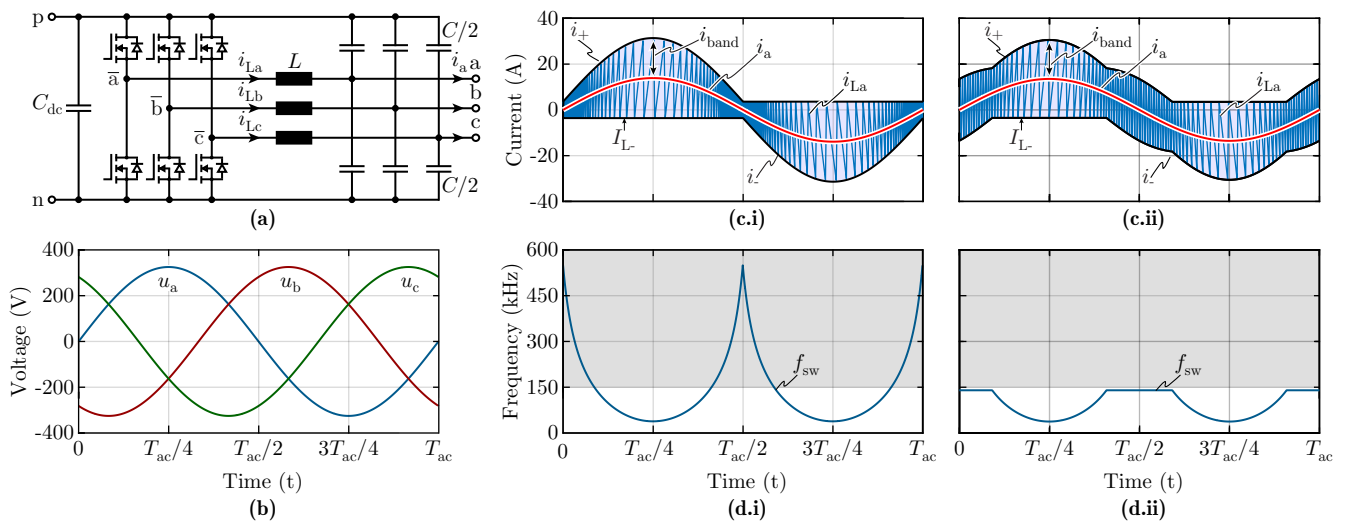
Fig. 1. (a) Three-phase DC/AC converter implemented with 2-level bridge-legs and an LC output-filter to generate (b) a symmetrical three-phase voltage system at the terminals a, b and c. (c) The positive (i_+) and negative (i_-) current limits and the average phase current (i_a) define the inductor current, i_{La} and (d) the local switching frequency f_{sw} over the ac period $T_{ac} = 1/f_{ac}$ for (i) the conventional TCM and (ii) the introduced B-TCM modulation strategies. The latter approach prevents fundamental switching frequency components within the restricted spectrum (grey shaded area, above 150 kHz) of CISPR 11 [3].

phase. This structure supports both the direct paralleling (and interleaving) of additional bridge-legs [22] and low-complexity control, and leaves open the possibility of a third harmonic injection [23] (as discussed in **Appendix A** and introduced later). This modularity and simplicity is preferred over a coupled filter structure in many applications, including for the focus of this paper: unity power factor operation without a third harmonic.

A way to ensure a TCM modulation that enables ZVS over the full line cycle while still featuring sinusoidal currents is to add and subtract a current band i_{band} to the (reference) mains current i_a (cf., **Fig. 1c**) in such a way that the upper i_+ and lower i_- current bounds of the current envelope are defined as:

$$\begin{cases} i_+(t) &= i_a(t) + i_{band}(t) \geq 0 \\ i_-(t) &= i_a(t) - i_{band}(t) \leq 0, \end{cases} \quad (1)$$

where to guarantee ZVS for all operating cases, i_+ and i_- can also be kept (sufficiently) positive and negative for the full line cycle [10]. In TCM, the soft-switching portion of the current envelope (i_+ for the first half and i_- for the second half of the line cycle in **Fig. 1(c.i)**) is set with a fixed value $|I_{L-}|$, defining the band as $i_{band}(t) = |i_a(t)| + |I_{L-}| > 0$ A. The resulting current bands and average output current are shown in **Fig. 1(c.i)**.

This state-of-the-art TCM approach (see **Fig. 1(c.i)**) [24] achieves ZVS across the full mains cycle but incurs a large variation in switching frequency, where the maximum frequency is only limited by the turn-off current, I_{L-} (assuming the current and voltage are in phase). For the converter specifications here (**Table I**) with the required inductance ($L = 53\,\mu H$) and a turn-off current of $I_{L-} = -3.5$ A,

the minimum switching frequency is 40 kHz and the maximum switching frequency is 540 kHz, an enormous $15\times$ variation in switching frequency (**Fig. 1(d.i)**). This frequency variation – and especially the high frequencies near the zero-crossing of i_a – complicates the filter design, especially with the regulations on emissions above 150 kHz [3] and represents

a challenge with regard to the practical implementation of the current control. Prior art has limited the switching frequency in three-phase AC-DC power converters by synchronizing the switching frequency across the three phases under critical conduction mode modulation [19,25]–[27], by employing variable space vector modulation control [28], by clamping the switching frequency to a particular boundary [23], and by fixing the bandwidth of the modulation scheme to a constant value across the full mains cycle [29,30].

A solution is sought, then, that maintains ZVS while lowering the maximum switching frequency, reduces the overall variation across the line cycle, can be applied to single-phase or decoupled three-phase systems, and takes the residual (non-zero) ZVS losses into consideration for the semiconductor optimization. In this paper, we first introduce a bounded triangular-current-mode (B-TCM) modulation scheme (see **Fig. 1(c.ii)**), where the switching frequency is limited to, say, 140 kHz, but ZVS is still guaranteed across the mains cycle. The B-TCM approach is then extended to a sinusoidal triangular-current-mode, or S-TCM, modulation scheme with a constant current band of $i_{band}(t) = \hat{I}_{max}$, where $\hat{I}_{max}$ is the maximum rated current amplitude of the converter system. The proposed S-TCM scheme achieves ZVS across the full mains period, like TCM, but also limits the maximum switching frequency to, for example, 140 kHz (see **Fig. 2(b)**). In the end, as we show, S-TCM results in a significant reduction in filter requirements (nearly $5\times$ lower required inductance than CCM) while maintaining high bridge-leg efficiency, pushing AC-DC power conversion towards both high efficiency and high power density.

In **Section II**, the B-TCM modulation scheme is introduced and analyzed before its extension to the proposed S-TCM approach, which is comprehensively analyzed under three specific modulation approaches. In **Section III**, we measure the soft-switching losses of a 1200 V SiC MOSFET to analytically calculate actual semiconductor losses under S-TCM modulation. These calculations are experimentally validated with a hardware prototype in **Section IV**, with excellent matching
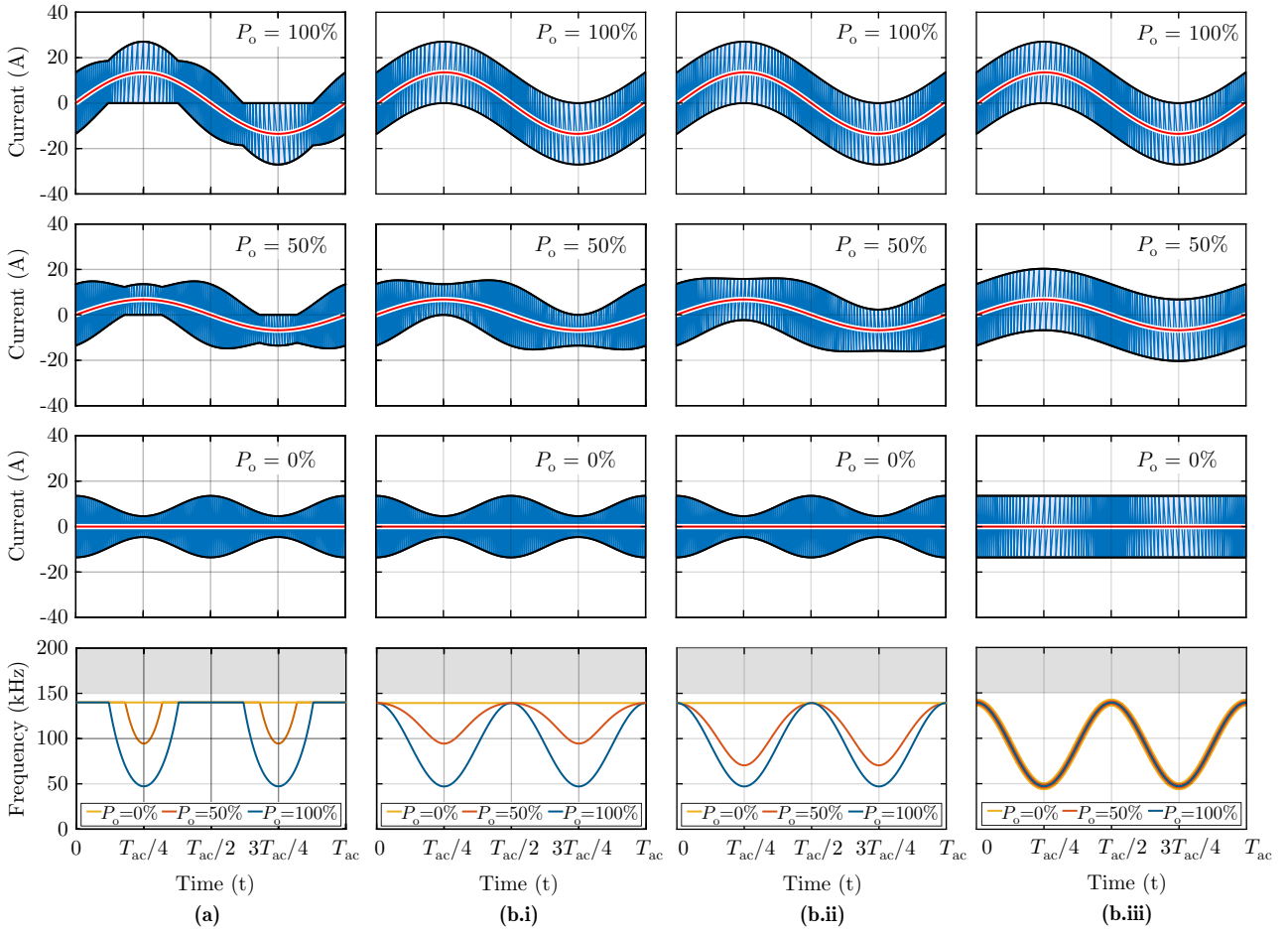
Fig. 2. The average phase current i_a and the inductor current i_{La} over the AC period T_{ac} for full-load, i.e. $P_o = 100\%$, part-load, i.e. $P_o = 50\%$, and no-load, i.e. $P_o = 0\%$, and the corresponding local switching frequencies f_{sw} for **(a)** B-TCM modulation scheme and **(b)** the three considered implementations of the S-TCM modulation scheme, **(i)** S-TCM$_i$, **(ii)** S-TCM$_{ii}$ and **(iii)** S-TCM$_{iii}$, for $L = 53\,\mu$H and $f_{sw,max} = 140\,$kHz.

Table I
DC-AC converter specifications.

$P_{o,max(3\text{-}\Phi)}$	U_{dc}	U_{ac}	ω_{ac}	L
6.6 kW	800 V	230 V$_{rms}$	2π 50 Hz	53 µH

between estimated and measured losses. Afterwards, **Section V** compares the performance and key characteristics of the novel S-TCM modulation to the conventional CCM and TCM modulation schemes, concluding that S-TCM outperforms both CCM and TCM in terms of efficiency. Finally, **Section VI** summarizes the findings of the paper.

II. B-TCM AND S-TCM ANALYSIS

Firstly, the state-of-the-art TCM solution with a large frequency variation is investigated and extended to the bounded TCM (B-TCM) modulation (shown in **Fig. 1(d.ii)**), where the switching frequency is bounded by an upper limit but ZVS is maintained. We reiterate here that the analysis of a single phase of the 3-Φ system is sufficient due the uncoupled phase filter structure.

Assuming a sinusoidal phase voltage, (i.e. $u_a(t) = \sqrt{2}U_{ac}\sin(\omega_{ac}t)$) and a constant DC-link voltage U_{dc}, we can

define the modulation index:

$$M = \frac{\sqrt{2}U_{ac}}{U_{dc}/2} = 0.81. \tag{2}$$

Generally, the on- and off-times of the high-side switch are:

$$\begin{cases} t_{on}(t) = \frac{2L\Delta i_L(t)/U_{dc}}{1 - M\sin(\omega_{ac}t)} \\ t_{off}(t) = \frac{2L\Delta i_L(t)/U_{dc}}{1 + M\sin(\omega_{ac}t)}, \end{cases} \tag{3}$$

with the time-dependent peak-to-peak current ripple Δi_L and with $T_{sw}(t) = t_{on}(t) + t_{off}(t) = 1/f_{sw}(t)$; the switching frequency is:

$$f_{sw}(t) = \frac{U_{dc}}{4L\Delta i_L(t)} \cdot \left[1 - M^2\sin^2(\omega_{ac}t)\right]. \tag{4}$$

We can now analyze the switching frequency variation for different choices of current bands. In particular, the band can be modulated according to different side conditions, while ensuring *(a)* the maximum frequency limitation and *(b)* ZVS across the full mains cycle. Under the proposed modulation schemes, it should be noted, a minimum turn-off current of $0\,$A may occur within the mains cycles. With $0\,$A turn-off current, however, ZVS is only guaranteed for inverter operation (DC-AC) with $\cos\phi = 1$. For rectifier operation, however, a minimum turn-off current $I_{min} \leq |I_{L\text{-}}|$ is required to ensure full ZVS (according to the $u - Zi$ diagram analysis [14]):
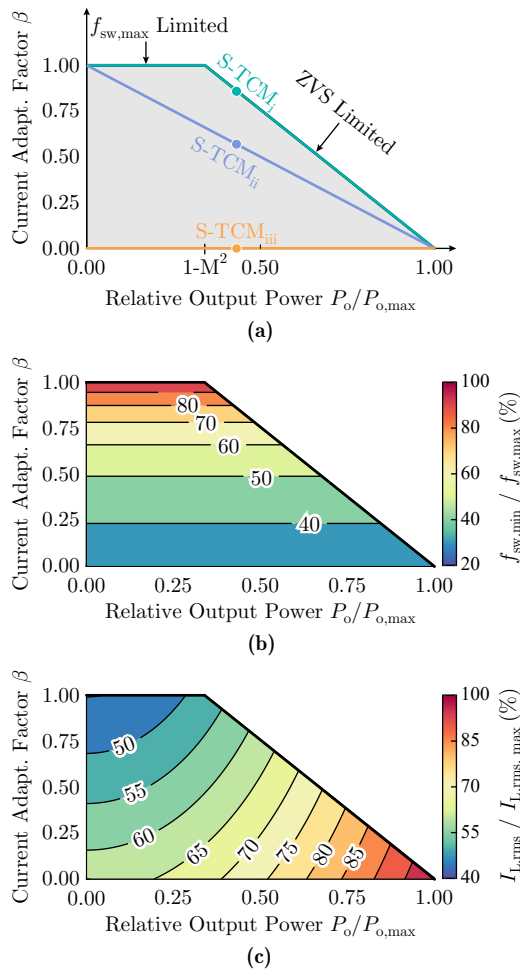
(a)

(b)

(c)

Fig. 3. (a) S-TCM modulation area limited by the maximum switching frequency $f_{\text{sw,max}}$, i.e. $\beta \leq 1$, and the ZVS limit to ensure ZVS under all operating conditions, with indicated paths for the implementation of S-TCM$_\text{i}$, S-TCM$_\text{ii}$ and S-TCM$_\text{iii}$. **(b)** Minimum switching frequency within the allowed modulation area across current band weighting β. **(c)** Inductor rms current, as a ratio of the inductor rms current at full load, across the S-TCM operating area. The conduction-loss-optimal S-TCM$_i$ implementation minimizes the rms current for a particular load.

$$I_{\min} = \frac{\sqrt{M} U_{\text{dc}}}{Z} \quad \text{with} \quad Z = \sqrt{\frac{L}{2 C_{\text{oss,Q}}}}, \quad (5)$$

where $C_{\text{oss,Q}}$ is the charge-equivalent output capacitance of the bridge-leg semiconductor. Further, the zero-crossing detector circuit [8] introduced later requires a small opposite-polarity current for correct operation. Because these effects are implementation-dependent, they are neglected in the theoretical analysis of the different modulation schemes but are revisited in **Section IV** for the experimental verification.

A. Bounded-TCM (B-TCM)

The state-of-the-art TCM modulation (see **Fig. 1(c.i)**) [24] uses the minimum current band to achieve ZVS with $i_{\text{band}}(t) = |i_\text{a}(t)| \geq 0\,\text{A}$, assuming a turn-off current requirement of $0\,\text{A}$, as mentioned before. Thus, this modulation scheme minimizes the inductor rms current and ensures the minimum achievable conduction losses for a TCM/ZVS system. By applying i_{band} to **Eqn. (4)**:

$$f_{\text{sw}}(t) = \frac{U_{\text{dc}}}{8L} \frac{1}{\hat{i}} \cdot \frac{1 - M^2 \sin^2(\omega_{\text{ac}} t)}{\sin(\omega_{\text{ac}} t)} > f_{\text{sw,max}}, \quad (6)$$

we can see that at angles close to $\omega_{\text{ac}} t = 0$, the instantaneous switching frequency f_{sw} is maximum. Therefore, if we want to limit $f_{\text{sw,max}}$ to, e.g., $140\,\text{kHz}$ (see **Fig. 1(d.i)**), the most intuitive solution is to directly bound the maximum switching frequency to $f_{\text{sw,max}}$, which we call bounded-TCM (B-TCM), which is active if $r(t) = \frac{f_{\text{sw}}(t)}{f_{\text{sw,max}}} \geq 1$, or:

$$f_{\text{sw}}(t) = \begin{cases} f_{\text{sw,max}} \cdot r(t) & \text{if} \quad r(t) < 1 \\ f_{\text{sw,max}} & \text{if} \quad r(t) \geq 1 \end{cases} \quad (7)$$

with

$$r(t) = \frac{f_{\text{sw}}(t)}{f_{\text{sw,max}}} = \frac{U_{\text{dc}}}{8L f_{\text{sw,max}}} \frac{1}{\hat{i}} \cdot \frac{1 - M^2 \sin^2(\omega_{\text{ac}} t)}{\sin(\omega_{\text{ac}} t)}. \quad (8)$$

B-TCM, we should note, can be implemented with only a simple zero-crossing detector and a calculation of the on-time of the high-side switch, with the on- and off-times selected under the constraint that a minimum period (corresponding to $f_{\text{sw,max}}$) is achieved.

The B-TCM implementation corresponds to an increase in the current band i_{band} in the intervals where $f_{\text{sw,max}}$ would otherwise be exceeded, which occurs near the average current zero crossings:

$$i_{\text{band}}(t) = \begin{cases} |i_\text{a}(t)| & \text{if} \quad r(t) < 1 \\ |i_\text{a}(t)| \cdot r(t) & \text{if} \quad r(t) \geq 1. \end{cases} \quad (9)$$

Fig. 2(a) shows the resulting current bands and the local switching frequency for difference load cases. It should be noted, that the frequency bounded interval, i.e. $f_{\text{sw}}(t) = f_{\text{sw,max}}$, is load-dependent and extends with reduced load currents, leading to a constant frequency modulation, similar to PWM operation, at no-load.

While B-TCM minimizes the rms inductor current and therefore the conduction losses under a maximum switching frequency, it suffers from a discontinuous implementation that complicates both the control and analysis, as well as from relatively high average switching frequency, which might generate larger semiconductor losses with non-negligible ZVS switching losses, as we explain in **Section III**. Therefore, the current envelope can be extended to a current band with continuous sinusoidal current boundaries, supporting system optimization from analytical closed-form expressions. In some cases, we note, the resulting current boundaries are close to the B-TCM results, as in **Fig. 2(a)** and **(b)**, and at zero load even identical.

B. Sinusoidal-TCM (S-TCM)

A solution is sought, then, that maintains ZVS, lowers the maximum switching frequency, and is implemented with continuous current bands. To fulfill these constraints, we propose a modulation scheme – named sinusoidal triangular-current-mode, or S-TCM – with a sinusoidal current band i_{band}. The S-TCM approaches achieve ZVS, like TCM, across the full mains period, but also limit the maximum switching frequency to, for example, $140\,\text{kHz}$ (to avoid the CISPR 11 band [3] starting at $150\,\text{kHz}$).

The band can be varied between the constant frequency modulation with $i_{\text{band,f}}(t) = |i_\text{a}(t)| \cdot r(t)$ and the constant current band modulation with $i_{\text{band,i}}$:

$$i_{\text{band,f}}(t) = \hat{I}_{\text{max}} \cdot \left[1 - M^2 \sin^2(\omega_{\text{ac}}t) \right] \quad (10)$$

$$i_{\text{band,i}}(t) = \hat{I}_{\text{max}}, \quad (11)$$

where $\hat{I}_{\text{max}}$ is the maximum rated current amplitude of the converter system. To allow the frequency to vary without exceeding $f_{\text{sw}}(t) = f_{\text{sw,max}}$, we now introduce a current band adaption factor β, that can be varied to move between the constant frequency current band ($\beta = 1$) and the constant current band ($\beta = 0$) (see **Fig. 3**):

$$i_{\text{band}}(t, \beta) = \hat{I}_{\text{max}} \cdot \left[1 - \beta M^2 \sin^2(\omega_{\text{ac}}t) \right]. \quad (12)$$

This current band factor, β, maps to output power level and can be considered as a knob to improve light-load efficiency by reducing the current ripple.

With an unrestricted choice of β for any output load, however, the ZVS condition may not be fulfilled if i_+ and i_- are not always positive and negative, respectively, for the whole mains period. With this second constraint, then, β must be limited to guarantee ZVS at all operating points as:

$$i_-(t) = i_a(t) - i_{\text{band}}(t, \beta) \leq 0 \, \text{A}. \quad (13)$$

Substituting the mains current i_a and **Eqn. (12)** into **Eqn. (13)** yields:

$$\hat{i} \sin(\omega_{\text{ac}}t) \leq \hat{I}_{\text{max}} \cdot \left[1 - \beta M^2 \sin^2(\omega_{\text{ac}}t) \right], \quad (14)$$

which has its critical operating case at $\sin \omega_{\text{ac}}t = 1$, where i_a is at its maximum and i_{band} at its minimum. At this point, the equation collapses to $\hat{i} < \hat{I}_{\text{max}} \cdot (1 - \beta M^2)$, leading to the ZVS constraint on β:

$$\beta \leq \frac{1}{M^2} \left(1 - \frac{\hat{i}}{\hat{I}_{\text{max}}} \right) = \frac{1}{M^2} \left(1 - \frac{P_o}{P_{\text{o,max}}} \right). \quad (15)$$

To fulfill the ZVS condition, then, β must be zero at the nominal power and, under the maximum frequency constraint, may be $\beta = 1$ at loads as high as $\frac{P_o}{P_{\text{o,max}}} = 1 - M^2$. These points are connected linearly, and this forms the allowed operating range of S-TCM modulation under the ZVS and maximum frequency constraints, as shown in **Fig. 3(a)**.

The local switching frequency is then:

$$f_{\text{sw}}(t, \beta) = \frac{U_{\text{dc}}}{8L\hat{I}_{\text{max}}} \cdot \frac{1 - M^2 \sin^2(\omega_{\text{ac}}t)}{1 - \beta M^2 \sin^2(\omega_{\text{ac}}t)}, \quad (16)$$

where as long as $\beta \leq 1$, $f_{\text{sw}}(t) \leq f_{\text{sw,max}}$. Since the maximum switching frequency was constrained in the original problem definition, f_{sw} still cannot exceed $f_{\text{sw,max}}$, as desired. At the current zero crossing ($w_{\text{ac}}t = n\pi$, with $n = 1, 2, 3...$) with $t_{\text{on}} = t_{\text{off}}$, i.e. a 50 % duty cycle, the maximum switching frequency occurs and is:

$$f_{\text{sw,max}} = \frac{U_{\text{dc}}}{8L\hat{I}_{\text{max}}}. \quad (17)$$

The minimum switching frequency, however, may now increase with β, and the switching frequency ratio is now

$$\frac{f_{\text{sw,max}}}{f_{\text{sw,min}}} = \frac{1 - \beta M^2}{1 - M^2}. \quad (18)$$

The minimum switching frequency $f_{\text{sw,min}}$ across the full β-load S-TCM operating area is shown in **Fig. 3(b)** and for our

application and with the choice of $f_{\text{sw,max}} = 140 \, \text{kHz}$ (resulting in an inductance value of $L = 53 \, \mu\text{H}$), $f_{\text{sw,min}} = 48 \, \text{kHz}$ and $f_{\text{sw,max}}/f_{\text{sw,min}} = 2.9$, a small overall variation relative to the $f_{\text{sw,max}}/f_{\text{sw,min}} = 15$ of traditional TCM modulation.

The β-load maps of **Fig. 3** outline the allowed S-TCM modulation area with the ZVS, continuity, and maximum switching frequency constraints. From here, we determine the analytical expressions for the switching losses and inductor current as a function of β to quantitatively compare the specific S-TCM modulation schemes.

1) Switching Losses: With current-dependent switching losses $E_{\text{sw}}(I_{\text{sw}})$, the local switching losses for the bridge-leg can be generally written as $p_{\text{sw}}(t) = f_{\text{sw}}(t) \cdot [E_{\text{sw}}(i_+(t)) + E_{\text{sw}}(i_-(t))]$. Under ZVS, the semiconductor losses can be described with a quadratic loss function of $E_{\text{sw}} = a + b|I_{\text{sw}}| + c|I_{\text{sw}}|^2$, a fitting found in [31] and [32] and further experimentally verified in **Section III**. The average of the local switching losses across the mains cycle is shown at the bottom of page in **Eqn. (19)**.

$$P_{\text{sw}}(\beta) = \frac{U_{\text{dc}}}{4L\beta^2 \hat{I}_{\text{max}}} \Bigg\{ \beta \left(1 - \frac{1 - \beta}{\sqrt{1 - \beta M^2}} \right) a +$$
$$\beta^2 \left(1 - \frac{M^2}{2} \right) b \hat{I}_{\text{max}} +$$
$$\beta^2 \left[1 - (1 + \beta) \frac{M^2}{2} + \frac{3\beta M^4}{8} \right] c \hat{I}_{\text{max}}^2 +$$
$$\left[\frac{\beta}{2} + \frac{1 - \beta}{M^2} \left(1 - \frac{1}{\sqrt{1 - \beta M^2}} \right) \right] c\hat{i}^2 \Bigg\} \quad (19)$$

2) Inductor Current: With the switching frequency and switching losses defined, only conduction losses remain to complete the analysis of the proposed S-TCM scheme. With the triangular shape of the inductor current i_L, the inductor rms current over a switching cycle is determined by the positive and negative current limits as $i_{\text{L,rms}}(t)^2 = \frac{1}{3} \left(i_+^2(t) + i_+(t)i_-(t) + i_-^2(t) \right)$, and can be used to calculate the global inductor rms current as $I_{\text{L,rms}}^2 = \frac{1}{T_{\text{ac}}} \int_0^{T_{\text{ac}}} i_{\text{L,rms}}(t)^2 \text{d}t$. With the considered current band of **Eqn. (12)**, the inductor rms current is:

$$I_{\text{L,rms}}(\beta) = \sqrt{\frac{\hat{i}^2}{2} + \frac{\hat{I}_{\text{max}}^2}{3} \left(1 - \beta M^2 + \frac{3\beta^2 M^4}{8} \right)}. \quad (20)$$

Fig. 3(b) shows the inductor rms current as a ratio of the current at full load, across the full β-load operating area. Bridge-leg conduction losses therefore follow as $P_{\text{cond}} = R_{\text{ds,on}} I_{\text{L,rms}}^2$.

While the above results consider zero phase-shift between the phase voltage and current and no third-harmonic injections, these assumptions are relaxed in **Appendix A** to extend the use cases of the proposed S-TCM scheme.

C. S-TCM Modulation Implementations

With the semiconductor losses and inductor rms current determined for the generalized S-TCM approach, we propose three specific S-TCM implementations with different benefits and downsides. All of these approaches can be implemented with only a zero-crossing detector [8] (i.e. high-bandwidth current measurements are not required) and a simple calculation of switch on- and off-times, as demonstrated in **Section IV**.

1) Concept S-TCM$_i$: Because $\beta M^2 \leq 1$ for all conditions, an increase in β always reduces the rms current, cf. **Fig. 3(c)**, and, therefore, the minimum conduction losses occur at the maximum β that is allowed under the particular load constraint, cf. **Fig. 2(b.i)**. The S-TCM modulation scheme achieving minimal conduction losses, also referred as S-TCM$_i$, then, is $\beta = 1$ for $\frac{P_o}{P_{o,max}} < 1 - M^2$ and a linear decrease with load to $\beta = 0$ at $P_o = P_{o,max}$. This conduction-loss-optimal S-TCM modulation is shown as the S-TCM bounding line in **Fig. 3(a)**.

2) Concept S-TCM$_{ii}$: Now, a simpler S-TCM modulation scheme S-TCM$_{ii}$ can be introduced with a continuous function that only depends on the load. Here, β is linearly adapted from 1 at no load to 0 at full-load, with the waveforms shown in **Fig. 2(b.ii)** and the β-load line shown in **Fig. 3(a)**.

While this scheme is not conduction loss minimizing, the implementation is straightforward, and, as we show in the next section, close to the *total* loss optimal modulation line.

3) Concept S-TCM$_{iii}$: Finally, S-TCM modulation with a constant current band ($i_{band}(t) = \hat{I}_{max}$, or $\beta = 0$) that is independent of the location in the mains cycle or the load shown in **Fig. 2(b.iii)** is proposed, the ripple is $\Delta i_L(t) = 2i_{band}(t) = 2\hat{I}_{max}$ for a local switching frequency of:

$$f_{sw}(t) = \frac{U_{dc}}{8L\hat{I}_{max}} \cdot \left[1 - M^2 \sin^2\left(\omega_{ac}t\right)\right]. \tag{21}$$

and the ratio simplifies to

$$\frac{f_{sw,max}}{f_{sw,min}} = \frac{1}{1 - M^2}. \tag{22}$$

Also the switching losses found for the S-TCM scheme in **Eqn. (19)**, can be simplified with $\beta = 0$ to

$$P_{sw} = \frac{U_{dc}}{4L\hat{I}_{max}}\left[\left(1 - \frac{M^2}{2}\right)\left(a + b\hat{I}_{max} + c\hat{I}_{max}^2\right) \right. $$
$$\left. + \frac{1}{2}\left(1 - \frac{3}{4}M^2\right)c\hat{i}^2\right], \tag{23}$$

where we see that most of the losses only depend on the maximum designed current $\hat{I}_{max}$ and only a small fraction are load-dependent ($\hat{i}$). Similarly, with $\beta = 0$ under the constant current bands proposed in this section, the inductor rms current is simply:

$$I_{L,rms} = \sqrt{\frac{\hat{i}^2}{2} + \frac{\hat{I}_{max}^2}{3}}, \tag{24}$$

which is the superposition of the average output current and a triangular high-frequency current with magnitude $\hat{I}_{max}$.

With B-TCM and three different implementations of S-TCM proposed and analyzed, we seek to minimize the total bridge-leg losses under the key constraints of ZVS, continuity in implementation, and a maximum switching frequency. This total loss minimization is the focus of the next section, where the measured switching losses in a low-$R_{ds,on}$ SiC MOSFET form the foundation of an analysis of the preferred S-TCM modulation scheme.
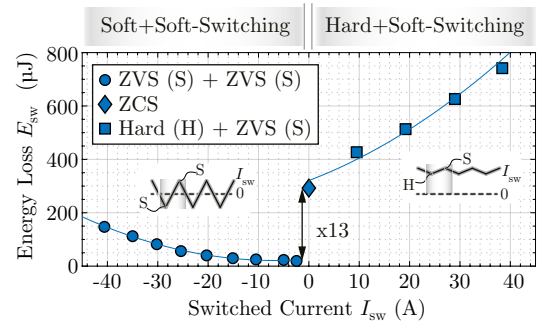

Fig. 4. Measured soft-switching losses E_{sw} of the *C3M0016120K* for a full bridge-leg ($U_{dc} = 800\,$V) across switched current I_{sw}. Hard-switching losses are reproduced from [31].

Table II
Fitted switching loss coefficients for a 1200 V SiC MOSFET (*C3M0016120K*) operated at $U_{dc} = 800\,$V, valid for $E_{sw} = a + b|I_{sw}| + c|I_{sw}|^2$.

Coefficient	Soft-Switched	Hard-Switched
a in μJ	12.9	312.9
b in μJ/A	-0.7	7.7
c in nJ/A^2	55.6	55.0

III. EXPERIMENTAL ANALYSIS

A. Switching Loss Characterization

To quantitatively analyze and predict the losses in an S-TCM modulated DC-AC converter with the specifications of **Table I**, the switching losses $E_{sw}(I_{sw})$ must be known for the selected power semiconductors. Here, we select the lowest-$R_{ds,on}$ SiC MOSFET from Cree's 3rd-generation family (*C3M0016120K*), a 16 mΩ and 1.2 kV device. The measured on-resistance at 60 °C of 18.09 mΩ is used for all of the following calculations.

The soft-switching losses of this device are measured in a calorimetric setup [32] (with adapted deadtimes to ensure complete soft-switching) and reported in **Fig. 4**, with the hard-switching losses from [31] included for completeness. Gating losses of 4.2 μJ per cycle are included in the switching losses, and total bridge-leg losses are shown for two conditions: two soft-switching transitions (S-TCM and other TCM schemes) and one hard- and one soft-switched transition (CCM).

Firstly, we underline the importance of soft-switching modulation schemes generally, as the losses at low soft-switched currents are 13× lower than the zero-current (minimum) hard-switching losses. Secondly, we see that the quadratic current-dependent loss formula ($E_{sw} = a + b|I_{sw}| + c|I_{sw}|^2$) fits both soft- and hard-switched losses accurately, with the fitted loss coefficients for a single hard or soft transition given in **Table II**. We reiterate that the current-independent coefficient a includes the gating losses of the MOSFET (4.2 μJ in this case), which are non-negligible for soft-switched converters.

For the operating conditions of **Table I** and the selected power device, **Eqn. (5)** gives a required turn-off current of 3.0 A to achieve full-ZVS across the full operating range. Similarly, the 200 ns delay in the implemented zero-crossing detector (ZCD) circuit [8] – including the transformer & comparator (80 ns), FPGA read-in and calculation (56 ns), gate driver propagation delay (24 ns), and switch turn-on time
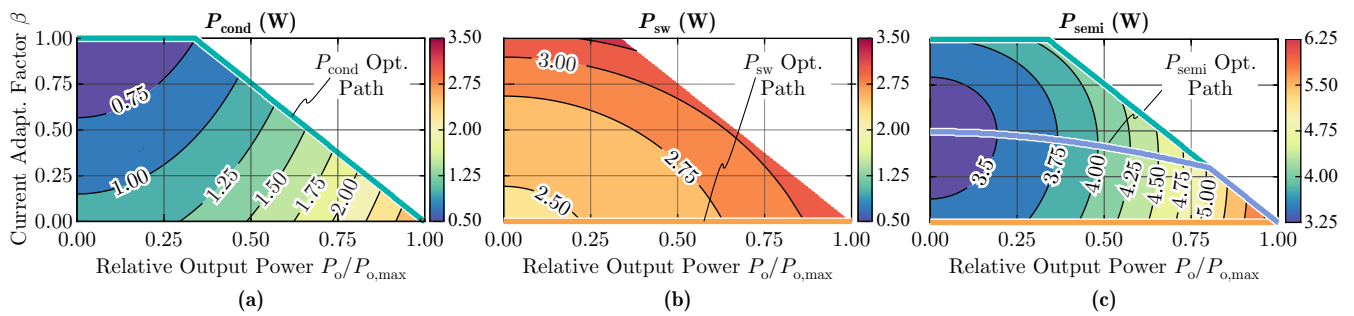
Fig. 5. **(a)** Conduction P_{cond}, **(b)** switching P_{sw}, and **(c)** total semiconductor losses P_{semi} evaluated over the full operating area. The x-axis is the load level as a ratio of the nominal power of 2.2 kW (see **Table I**) and the y-axis is the current adaption factor, β. For a given load, β can be selected to give the optimal conduction losses as shown by the load-dependent path in **(a)**, the optimal switching losses in **(b)**, or the optimal total semiconductor losses in **(c)**.
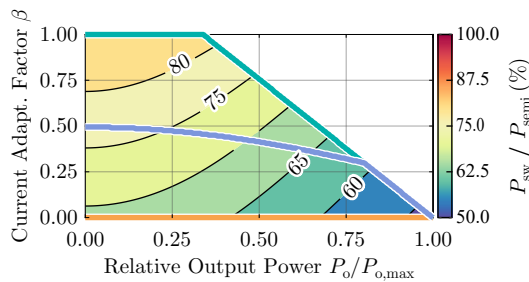

Fig. 6. Ratio of the switching losses to the total semiconductor losses $P_{\text{sw}}/P_{\text{semi}}$ over the full S-TCM modulation range. Optimal conduction, switching, and total semiconductor loss paths from **Fig. 5** are overlaid.

(40 ns) – require a minimum current of 2.8 A for correct operation. With these two constraints, a minimum soft-switched current of $I_{\text{L-}} = -3.5$ A is selected to include margin. This selected current is around 10 % of the peak inductor current, supporting the choice of the low-$R_{\text{ds,on}}$ power MOSFET.

B. Bridge-Leg Losses in S-TCM

With the switching losses of the selected device characterized as a function of switched current, the conduction P_{cond}, switching P_{sw}, and total semiconductor losses $P_{\text{semi}} = P_{\text{cond}} + P_{\text{sw}}$ are now evaluated across the full operating area of the S-TCM modulation concept under the specifications of **Table I**. These results are shown in **Fig. 5**.

As predicted in **Section II-C1**, the minimum conduction loss modulation scheme – under the maximum switching frequency and ZVS constraints – is to follow $\beta = 1$ until $\frac{P_{\text{o}}}{P_{\text{o,max}}} = 1 - M^2$ and then linearly decrease β to full load. This follows the intuition that the maximum possible β minimizes the current ripple and therefore the rms current. Across this load range, conduction losses (**Fig. 5(a)**) increase from 0.5 W at zero load and $\beta = 1$ to above 2.8 W at full load. If $\beta = 0$ was kept across the full cycle for minimum switching losses, the conduction losses at zero load would be more than 2× larger.

Fig. 5(b) shows the switching losses across the S-TCM regime, using the losses measured in (and coefficients derived from) **Fig. 4**. The switching-loss-optimal modulation path is not directly known, since higher β reduces the switched current (lower energy loss *per cycle*) but increases the switching frequency (see **Fig. 3(b)**). The relative importance of these will change on a device-by-device basis. For the selected MOSFET, the soft-switching losses are relatively flat with current (relatively small b and c coefficients, as given in **Table II**), and the path that minimizes switching losses is

$\beta = 0$ for the full load range. The switching losses vary from 2.5 W at zero load to nearly 3.5 W.

Finally, these loss contributions are combined in **Fig. 5(c)** for the total semiconductor losses, which vary between 3.4 W and 6.0 W. The total-loss-optimum modulation path is highlighted. This path is dependent on the particular power device, but for the SiC MOSFET chosen here, happens to fall near the S-TCM$_{ii}$ modulation scheme outlined in **Section II-C2**. This optimal modulation path will be highly device-dependent, and, further, we note that S-TCM$_{ii}$ may be preferred to S-TCM$_{iii}$ modulation with a constant current band outlined in **Section II-C3** for its ability to save cost with smaller (higher-$R_{\text{ds,on}}$) devices in some applications. In **Fig. 6**, the relative contributions from conduction and switching losses is delineated. At full load, the conduction and switching losses are nearly equal, with switching losses contributing the majority of the losses over the remainder of the S-TCM operating region.

At maximum output power, the S-TCM modulation scheme (at full load, the three specific approaches dovetail into one) results in 6.0 W of bridge-leg losses, with 2.8 W conduction and 3.2 W switching losses. The B-TCM implementation results in 5.7 W of semiconductor losses, divided into 2.3 W conduction and 3.4 W switching losses, with slightly lower rms currents but higher switching frequencies across the line cycle. With similar switch losses, the sinusoidal band is preferred for the implementation continuity.

In the next section, we move to validate these loss predictions in a full hardware demonstrator operating under multiple S-TCM modulation schemes, simultaneously showing the utility of the proposed modulation scheme (relative to CCM and TCM) and the accuracy of the loss estimates.

IV. MEASUREMENT RESULTS

The theoretical analysis of the S-TCM converter operation is verified by hardware measurements. The hardware prototype is a single-phase, 2.2 kW DC-AC converter (one phase of the structure of **Fig. 1(a)**) with the specifications of **Table I**, *C3M0016120K* SiC MOSFETs as the power semiconductors, and an L-C filter with $L = 52\,\mu$H and $C = 8.8\,\mu$F. We reiterate that the maximum switching frequency of 140 kHz is selected to avoid fundamental frequency components in the CISPR 11 band that starts at 150 kHz.

Since the theoretical model assumes zero transition times and no phase shift between the output phase and current (neither of which are strictly true), the filter inductance can
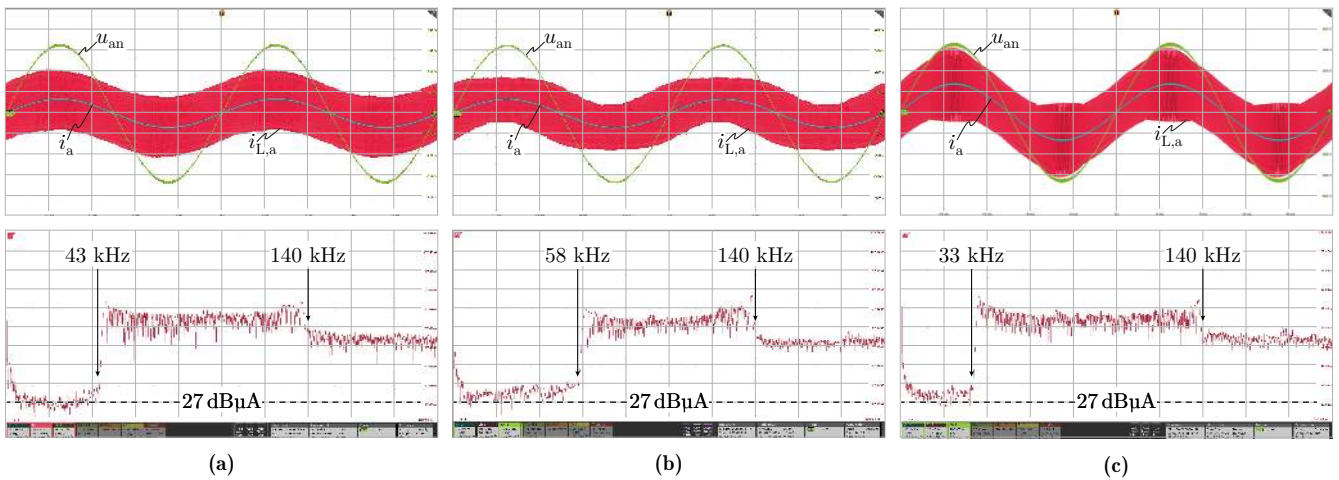
Fig. 7. Measured oscilloscope waveforms of phase voltage ($u_{a,n}$), phase current (i_a), and inductor current ($i_{L,a}$) for **(a)** 50% load under S-TCM$_{iii}$, with predicted rms current of 9.16 A and measured rms current of 9.40 A, **(b)** 50% load under S-TCM$_{ii}$, with predicted rms current of 8.13 A and measured rms current of 8.43 A, and **(c)** full load ($\beta = 1$), with predicted rms current of 12.32 A and measured rms current of 12.95 A. Measured fast Fourier transform (FFT) for the inductor current shown, with the maximum and minimum switching frequencies in each mode highlighted. Scale: $100\,\text{V/div}$, $10\,\text{A/div}$, $4\,\text{ms/div}$, $20\,\text{kHz/div}$ and $10\,\text{dB\mu A/div}$.

be reduced from the predicted $L = 53\,\mu\text{H}$ to $L = 52\,\mu\text{H}$ while maintaining a maximum switching frequency below $140\,\text{kHz}$ across the full operating range. An inductor design is selected from the optimal front of a Pareto optimization following the design guidelines proposed in [33] under the constraints of inductance value, saturation current, and thermal limits, and this selected inductor is implemented with 5 stacked E40/16/12 N87 cores with 12 turns of litz wire (765 strands x $71\,\mu\text{m}$) for a volume of $106\,\text{cm}^3$ and 6 W of expected losses at full power.

Measurements of the phase voltage ($u_{a,n}$), phase current (i_a), and inductor current ($i_{L,a}$) are given in **Fig. 7** for $50\,\%$ load under S-TCM$_{iii}$ with constant band (**Fig. 7(a)**), $50\,\%$ load under S-TCM$_{ii}$ (**Fig. 7(b)**), and full load (**Fig. 7(c)**) conditions (as mentioned above, the current band is increased for full load to meet the ZCD requirements). The prototype inverter is tested with a variable resistive load. At higher β for the same load – comparing S-TCM$_{ii}$ (**Fig. 7(b)**) to S-TCM$_{iii}$ (**Fig. 7(a)**) at $50\,\%$ load – the inductor rms current is lower for reduced conduction losses, reducing from $9.4\,\text{A}$ (S-TCM$_{iii}$, predicted at $9.16\,\text{A}$) to $8.43\,\text{A}$, predicted at $8.13\,\text{A}$ (S-TCM$_{ii}$). At full power, the rms current prediction error increases ($12.95\,\text{A}$ measured against $12.32\,\text{A}$ predicted) due to the additional current for soft-switching and the ZCD circuit operation (as detailed in **Section III**). For the full load operation, the current band is increased slightly near the current peak to ensure correct operation of the ZCD circuit and ZVS across the line cycle, resulting in a wider spectrum and a larger error between predicted and measured currents. Note the significant reduction in rms current at partial load when moving from S-TCM$_{iii}$ **(a)** to S-TCM$_{ii}$ **(b)**, resulting in higher light-load efficiency.

Additionally, the inductor current fast Fourier transform (FFT) is shown in **Fig. 7** for the three operating points. The switching frequency is, as desired, limited to $140\,\text{kHz}$, and the measured noise is lowered by around $20\,\text{dB}\,\mu\text{A}$ by the start of the EMI band at $150\,\text{kHz}$. The minimum switching frequency depends on the operating point (as shown in **Fig. 3(b)**), with these values also highlighted in **Fig. 7**. Theoretically, the frequency variation for **Fig. 7(a)** and **Fig. 7(c)**, which both
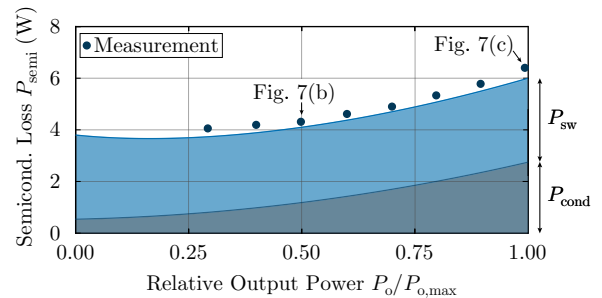

Fig. 8. Calculated and measured semiconductor bridge-leg losses in the hardware prototype operating with the proposed S-TCM$_{ii}$ approach. The total calculated losses P_{semi} are broken out into conduction losses P_{cond} and switching losses P_{sw}, and the measured semiconductor losses are shown as circles. The maximum error between predicted and measured losses is $0.3\,\text{W}$, for a bridge-leg loss estimation within $10\,\%$ across the load range and modulation scheme.

have $\beta = 0$, should be the same, but the spectrum is wider at full load (**Fig. 7(c)**) to the increased bands for the ZCD circuit and soft-switching operation. We note that, while the frequency variation is much smaller than under traditional TCM operation (**Fig. 1(d.i)**), this $3\times$ variation in switching frequency still introduces spread spectrum harmonics (e.g. fundamental from $50\,\text{kHz}$ to $140\,\text{kHz}$, 2$^{\text{nd}}$ harmonic from $100\,\text{kHz}$ to $280\,\text{kHz}$, etc.) that overlap with the regulatory band and complicate the EMI filter design.

For a grid-tied application, the filter capacitor C is selected such that the high-frequency voltage ripple is below $1\,\%$ of the fundamental amplitude, corresponding to $4.5\,\mu\text{F}$. With the assumption of isolated heat sinks and negligible parasitic switch-node to earth capacitances, a 2$^{\text{nd}}$ EMI filter stage with a cutoff frequency of $35\,\text{kHz}$ would be needed to attenuate the remaining differential and common mode noise ($104\,\text{dB\mu V}$ located at $150\,\text{kHz}$) by $25\,\text{dB}$ to meet CISPR Class A.

Finally, the loss estimates of **Section III** are verified across output load for the S-TCM converter prototype operating in S-TCM$_{ii}$. **Fig. 8** shows the predicted and measured (based on a calorimetric setup [32]) losses, with the calculated losses broken out into separate conduction and switching losses. The
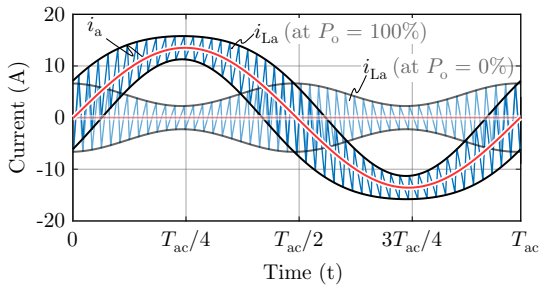
Fig. 9. Simulated inductor ($i_{L,a}$) and average output (i_a) current waveforms in a CCM bridge-leg with a switching frequency of $48\,\text{kHz}$ and an inductor of $315\,\mu\text{H}$ at full load and zero load.

error between the measured and calculated losses is below $10\,\%$ or $0.3\,\text{W}$, an excellent matching for the proposed theory. This small error is attributed to diode conduction losses and the current band increase near full load.

The measured bridge-leg efficiency reaches over $99.7\,\%$ at the nominal load, with S-TCM$_\text{ii}$ benefiting from lower conduction losses but incurring higher switching losses at partial load. With a weaker dependence on the temperature coefficient of the MOSFET on-resistance, the S-TCM$_\text{ii}$ implementation will be preferred over S-TCM$_\text{iii}$ in applications with a large temperature range or significant self-heating.

For three-phase systems operating with the proposed S-TCM modulation schemes, a third harmonic can be injected, supporting a $15\,\%$ higher output voltage [34] with reduced frequency variation (between $70\,\text{kHz}$ to $140\,\text{kHz}$ at full load). S-TCM operation with third harmonic injection and operation with phase-shifted currents (i.e. non-zero phase between the phase voltage and current) are detailed in **Appendix A**.

V. COMPARISON TO CCM AND TCM

Finally, the experimentally-validated S-TCM performance of a bridge-leg and output filter must be compared to the conventional CCM approach to validate the benefits of the proposed modulation scheme. The inductor current and average output current under CCM modulation at full load and zero load are shown in **Fig. 9**.

The CCM converter switching frequency is selected at $48\,\text{kHz}$, which keeps the 3rd harmonic below $150\,\text{kHz}$, and a current ripple with an rms value of $20\,\%$ of the low-frequency amplitude $\hat{i}_\text{max}$ is assumed, leading to a required inductance of $315\,\mu\text{H}$. Again, the inductor is selected through a Pareto optimization following the design guidelines proposed in [33], and a constant loss design (relative to the implemented S-TCM inductor) is selected for $6\,\text{W}$ of inductor losses (same as for S-TCM operation, cf. **Section IV**). The required volume is $167\,\text{cm}^3$ (2 stacked U 30/25/16 N87 cores with 27-turn litz wire of 324 strands x $0.1\,\text{mm}$) for a volume increase over the S-TCM inductor of $58\,\%$.

Here, a filter capacitor C of $2.6\,\mu\text{F}$ is required to limit the high-frequency ripple to $1\,\%$ of the fundamental amplitude. In this case, the 2nd EMI filter stage would have a cutoff frequency of $75\,\text{kHz}$ to damp $16\,\text{dB}$ at $192\,\text{kHz}$. While this may result in a slightly smaller second stage than under S-TCM, any volume reduction here will be dwarfed by the $58\,\%$ volume penalty of the filter inductor L (the S-TCM inductor design details are given in **Section IV**).
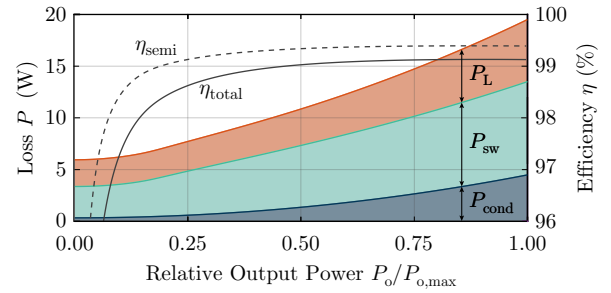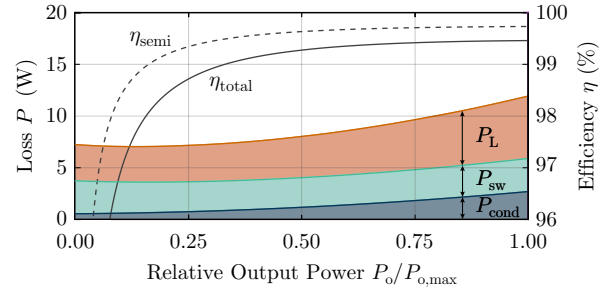
Fig. 10. Predicted losses across load for **(a)** the CCM benchmark, with a switching frequency of $48\,\text{kHz}$ and an inductor of $315\,\mu\text{H}$ and for **(b)** the S-TCM hardware prototype operating in S-TCM$_\text{ii}$ mode (semiconductor losses from **Fig. 8**) and an inductor of $52\,\mu\text{H}$.

The semiconductor losses in the proposed CCM comparison are calculated using **Table II**, assuming a continuous chip area to select the optimal die size at the maximum output power, following the scaling proposed in [35]. For the optimized $36\,\text{m}\Omega$ device, $13.4\,\text{W}$ of semiconductor losses occur at maximum power ($4.4\,\text{W}$ conduction losses, $9.0\,\text{W}$ switching losses), more than double the measured losses at full load with S-TCM modulation. Increasing the CCM switching frequency to $72\,\text{kHz}$ still renders the legacy modulation scheme noncompetitive, with the inductor volume penalty of $60\,\%$ and $3\times$ higher bridge-leg losses ($18\,\text{W}$ at an optimized die area corresponding to a $40\,\text{m}\Omega$ on-resistance) than under S-TCM.

The total losses under CCM and S-TCM are compared in **Fig. 10**, respectively, combining the inductor (P_L), switching (P_sw), and conduction (P_cond) losses across load. For the CCM modulation scheme (**Fig. 10(a)**), the peak efficiency is $99.1\,\%$ total with a bridge-leg efficiency of $99.4\,\%$. For the proposed S-TCM approach (**Fig. 10(b)**), the peak efficiency is $99.5\,\%$ total with a bridge-leg efficiency of $99.7\,\%$. While both concepts result in a similar EMI filter requirement, the semiconductor losses in the proposed S-TCM modulation are $55\,\%$ smaller smaller than with CCM while at the same time featuring a more compact filter inductor realization (cf., **Table III**). Finally, we can also compare the proposed S-TCM modulation scheme with conventional TCM modulation. As highlighted in **Section I** and **Fig. 1**, TCM modulation achieves soft-switching but at the expense of a large switching frequency variation, including operating above the $150\,\text{kHz}$ EMI regulatory limit [3] for part of the line cycle. The inductance value is selected to be $42\,\mu\text{H}$, such that the minimum switching frequency is the same as in S-TCM ($48\,\text{kHz}$, cf., **Table III**), leading to a frequency peak of of $684\,\text{kHz}$. In order to meet the

Table III
Comparison between modulation schemes for AC-DC power conversion under the specifications of **Table I** and designs evaluated here. Inductor and semiconductor losses are given at nominal power.

	CCM	TCM	S-TCM
Minimum f_{sw}	48 kHz	48 kHz	48 kHz
Peak f_{sw}	48 kHz	684 kHz	140 kHz
f_{sw} Variation	1×	14.3×	3×
$R_{ds,on}$	36 mΩ	16 mΩ	16 mΩ
P_{cond}	4.4 W	2.7 W	2.8 W
P_{sw}	9.0 W	5.2 W	3.2 W
Required Inductance	315 µH	42 µH	53 µH
Inductor volume	167 cm^3	107 cm^3	106 cm^3
Inductor losses	6.0 W	5.9 W	6.0 W

high-frequency output voltage ripple requirement of 1% of the fundamental amplitude, a filter capacitor C of $4.6\,\mu F$ is required. The 2nd EMI filter stage would require a cutoff frequency of $22\,kHz$ to attenuate $33\,dB$ at $150\,kHz$, which is approximately $10\,dB$ more than for the S-TCM and hence, increases the final volume of the EMI-filter. In addition to these additional EMI constraints, the large switching frequency variation complicates the digital control implementation and the inductor design. TCM designs, further, incurs higher switching losses than the proposed S-TCM scheme, i.e. $5.2\,W$ instead of $3.2\,W$, due to the higher switching frequency near the zero crossings.

Table III summarizes the results of the comparison between CCM, for which an optimal device selection with a die area corresponding to a $36\,m\Omega$ on-resistance is used for the calculation, and TCM and the proposed S-TCM modulation, both using the $16\,m\Omega$ device used in this work which features a good trade-off for soft-switched applications between the minimum required ZVS turn-off current (which increases for increasing die area) and conduction losses (which decrease with increasing die area). For a common baseline among the compared modulation schemes, we reiterate that we choose the minimum switching frequency of the TCM and S-TCM to be the same by adapting the inductance value of the TCM case, and we select the inductors such that they can be realized with the smallest volume while limiting the losses to $6.0\,W$.

VI. CONCLUSION

The proposed S-TCM scheme achieves both higher efficiency and lower volume (due to the lower required filter inductance) compared to CCM. With the ability to zero-voltage-switch over the full mains cycle, the continuous current band implementations, and the maximum frequency limit, the proposed S-TCM scheme addresses many of the shortcomings of both hard-switched (CCM) and soft-switched (TCM) modulation approaches for AC-DC power conversion. Further, this scheme supports phase modularity to scale to higher power levels and inherently includes both common- and differential-mode filtering.

Alternative concepts for 3-Φ, soft-switched converters do not inherently filter common-mode (although the CM noise is analyzed in [36]), but these approaches are promising [16, 18] and should be evaluated directly against the proposed S-TCM scheme on switching losses, conduction losses, and filter

volume and losses with both differential- and common-mode filtering. Only this complete, robust comparison can determine the right soft-switched modulation scheme to replace CCM in this critical power conversion application suite.

APPENDIX A
SINUSOIDAL MODULATION AND THIRD HARMONIC INJECTION UNDER S-TCM

To extend the proposed modulation schemes to a broader suite of applications, operation under two additional conditions is detailed here. Firstly, sinusoidal modulation with a phase-shifted current is considered to extend the schemes to, for example, motor drives, where it is typical for the current and voltage not to be fully in-phase, or grid-connected applications where reactive power compensated is required. We then detail third harmonic injection, which adds a zero-sequence component to the voltages generated against the DC-link midpoint without impacting the sinusoidal line-to-line voltages in 3-Φ systems.

A. Sinusoidal Modulation with Phase-Shifted Current

We consider a phase shift between the ac voltage and ac current such that $i_a(t) = \hat{i}\sin(\omega_{ac}t + \phi)$. The current band, though, is only dependent on the maximum current, so the phase shift has no influence, and the current band is still given by **Eqn. (12)** and the local switching frequency is still given by **Eqn. (16)**. The current limits i_+ and i_-, however, change and, with $\phi = 0$ as the worst-case for guaranteeing ZVS, the operating area can be extended for $\cos\phi < 1$.

With the phase shift, the rms current remains identical and is still given by **Eqn. (20)**. Following the same derivation for switching losses that is used in **Section II** leads to, for an arbitrary phase-shift ϕ and $\beta = 0$:

$$P_{sw}(\beta = 0, \phi) = \frac{U_{dc}}{4L\hat{I}_{max}}\left[\left(1 - \frac{M^2}{2}\right)\left(a + b\hat{I}_{max} + c\hat{I}_{max}^2\right) + \frac{1}{2}\left(1 - \frac{2 + \cos(2\phi)}{4}M^2\right)c\hat{i}^2\right] \quad (25)$$

and, across β:

$$P_{sw}(\beta, \phi) = \frac{U_{dc}}{4L\beta^2\hat{I}_{max}}\left\{Aa + Bb\hat{I}_{max} + Cc\hat{I}_{max}^2 + Dc\hat{i}^2\right\} \quad (26)$$

with:

$$A = \beta\left(1 - \frac{1-\beta}{\sqrt{1-\beta M^2}}\right),$$
$$B = \beta^2\left(1 - \frac{M^2}{2}\right),$$
$$C = \beta^2\left[1 - (1+\beta)\frac{M^2}{2} + \frac{3\beta M^4}{8}\right],$$
$$D = \frac{\beta}{2} + \frac{1-\beta}{M^2}\left(\cos(2\phi) + \frac{(\beta M^2 - 2)\cos(2\phi) - \beta M^2}{2\sqrt{1-\beta M^2}}\right).$$

The phase shift only influences the coefficient D and, for $\phi = 0$, the equations collapse to **Eqn. (19)** or **Eqn. (23)**.

For a given current amplitude, $\hat{i}$, a phase shift (or reduction in $\cos(\phi)$) leads to an increase in the switching losses, as a
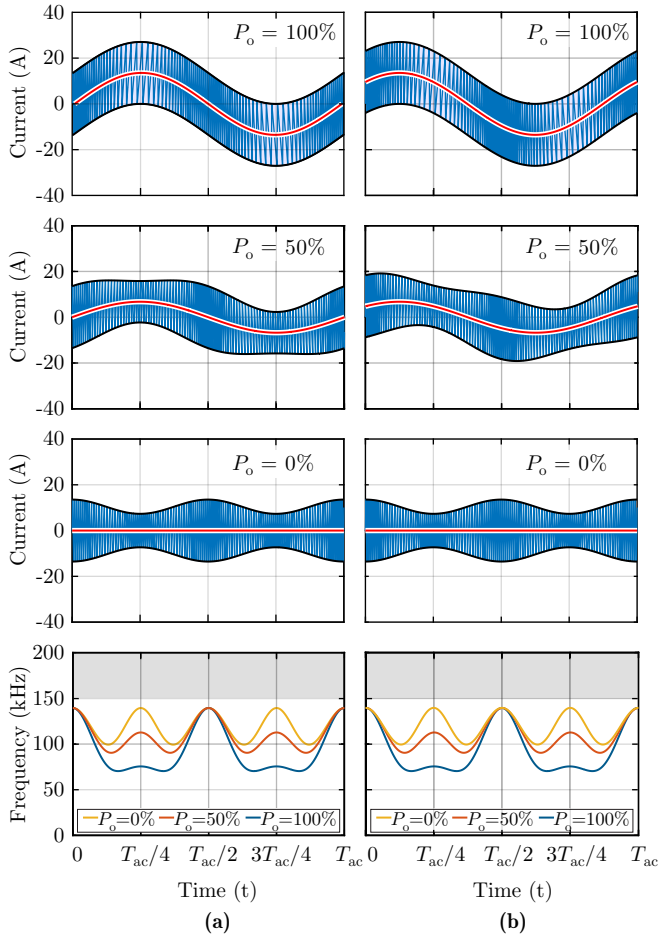
Fig. 11. The average phase current i_a and the inductor current i_{La} over the AC period T_{ac} for full-load ($P_o = 100\%$), partial load ($P_o = 50\%$), and no-load ($P_o = 0\%$) conditions, and the corresponding local switching frequencies f_{sw} considering a third harmonic voltage component under S-TCM$_{ii}$ **(a)** without a phase-shift and **(b)** with a phase-shift of $\phi = 45°$.

higher instantaneous current occurs at the switching frequency maximum. For the specifications considered here (see **Table I**) and the maximum output current of $\hat{i} = \hat{I}_{max}$, a maximum switching loss *increase* of 14% occurs for $\phi = \pm 90°$.

B. Third Harmonic Injection with Phase-Shifted Current

To increase the modulation index in 3-Φ systems without affecting the sinusoidal shape of the line-to-line voltages (which define, for example, the mains or motor current), we superimpose a harmonic voltage component with $3\times$ the ac frequency. The amplitude of the harmonic component is selected as $M/6$ in order to achieve the maximal possible modulation index of $M = \frac{2}{\sqrt{3}} \approx 1.15$ (under the side condition of sinusoidal phase-to-phase voltages) [37].

Under these third harmonic injection conditions, the phase voltage is $u_a(t) = MU_{dc}\sin(\omega_{ac}t) + \frac{M}{6}U_{dc}\sin(3\omega_{ac}t)$ and the corresponding current is $i_a(t) = \hat{i}\sin(\omega_{ac}t + \phi)$. The resulting switching frequency, following the derivation in **Section II**, is:

$$f_{sw}(t,\beta) = \frac{U_{dc}}{8L\hat{I}_{max}} \cdot \frac{1}{36[1 - \beta M^2 \sin^2(\omega_{ac}t)]} \cdot$$
$$[36 - 36M^2\sin^2(\omega_{ac}t) - M^2\sin^2(3\omega_{ac}t) + 6M^2\cos(4\omega_{ac}t) - 6M^2\cos(2\omega_{ac}t)], \quad (27)$$

This switching frequency waveform is shown in **Fig. 11**, where we see two local maximas at $\omega_{ac}t_i = n\pi$ and $\omega_{ac}t_{ii} = \frac{\pi}{2} + n\pi$ with $n \in \mathbb{Z}$, as:

$$f_{sw,max,i}(t_i, \beta) = f_{sw,max} = \frac{U_{dc}}{8L\hat{I}_{max}} \quad (28)$$

$$f_{sw,max,ii}(t_{ii}, \beta) = f_{sw,max} \cdot \frac{1 - \frac{25}{36}M^2}{1 - \beta M^2}. \quad (29)$$

To continue to ensure $f_{sw}(t, \beta) < f_{sw,max}$, β must be restricted to values below $25/36 \approx 0.69$ (or, equally, $\beta = 25/36$ corresponds to $f_{sw,max} = f_{sw,max,i} = f_{sw,max,ii}$). To consider S-TCM$_{ii}$ under third harmonic injection, then, the modulation scheme behavior can be re-derived with $\beta = \frac{25}{36}\left(1 - \frac{\hat{i}}{\hat{I}_{max}}\right)$, with the corresponding waveforms shown in **Fig. 11**. Again following the derivations of **Section II** (and with the same rms current, which is independent of ϕ), we find switching losses of:

$$P_{sw}(\beta = 0, \phi) = \frac{U_{dc}}{576L\hat{I}_{max}}\left[(144 - 74M^2)\left(a + b\hat{I}_{max} + c\hat{I}_{max}^2\right) + \right.$$
$$\left. (72 - 37M^2 - 12M^2\cos(2\phi))c\hat{i}^2\right] \quad (30)$$

and, with an arbitrary β:

$$P_{sw}(\beta, \phi) = \frac{U_{dc}}{576L\beta^4\hat{I}_{max}M^6} \cdot \quad (31)$$
$$\left\{Aa + Bb\hat{I}_{max} + Cc\hat{I}_{max}^2 + 2[D + E\cos(2\phi)]c\hat{i}^2\right\}$$

with:

$$A = 4\beta M^2\left(16 - 64\beta M^2 + 51\beta^2 M^4\right) +$$
$$4\beta M^2\left(\frac{-16 + 72\beta M^2 - 81\beta^2 M^4 + 36\beta^3 M^4}{\sqrt{1 - \beta M^2}}\right),$$
$$B = 2\beta^4 M^6\left(72 - 37M^2\right),$$
$$C = \beta^4 M^6\left(144 - 74M^2 - 72\beta M^2 + 49\beta M^4\right),$$
$$D = 16\beta M^2 - 64\beta^2 M^4 + 51\beta^3 M^6 +$$
$$\frac{-16\beta M^2 + 72\beta^2 M^4 - 81\beta^3 M^6 + 36\beta^4 M^6}{\sqrt{1 - \beta M^2}},$$
$$E = 32 - 144\beta M^2 + 166\beta^2 M^4 - 72\beta^3 M^4 - 14\beta^3 M^6 +$$
$$\frac{160\beta M^2 - 234\beta^2 M^4 + 72\beta^3 M^4 + 81\beta^3 M^6 - 36\beta^4 M^6 - 32}{\sqrt{1 - \beta M^2}}.$$

At the maximum output current and with no phase-shift (**Fig. 11(a)**), the switching losses are almost identical to the case without a third-harmonic-voltage component (around $3.2\,\text{W}$ per phase). The relative increase of switching losses across phase shift and output power under third harmonic injection is shown in **Fig. 12**, with the maximum of 10% for the considered design occurring again at $\hat{i} = \hat{I}_{max}$ and $\phi = \pm 90°$.
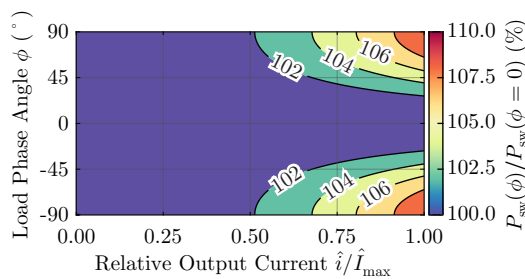
Fig. 12. Switching losses at different load phase angles ϕ relative to the switching losses at $\phi = 0°$ over output current with a third harmonic voltage component under the modulation scheme of S-TCM$_{ii}$. Considered operating parameters as given in **Table I**.

REFERENCES

[1] IEEE 1547, "Standard for Interconnecting Distributed Resources with Electric Power Systems," 2008.

[2] IEEE 519, "IEEE Recommended Practices and Requirements for Harmonic Control in Electrical Power Systems," 1993.

[3] CISPR 11, "Industrial, Scientific and Medical (ISM) Radio-Frequency Equipment – Electromagnetic Disturbance – Characteristics Limits and Methods of Measurement," 2009.

[4] BDEW Stdandard, "Technical Guideline Generating Plants Connected to the Medium-Voltage Network," 2008.

[5] D. O. Boillat, T. Friedli, J. Mühlethaler, J. W. Kolar, and W. Hribernik, "Analysis of the Design Space of Single-Stage and Two-Stage LC Output Filters of Switched-Mode AC Power Sources," in *Proc. of IEEE Power and Energy Conference at Illinois (PECI)*, Champaign, IL, USA, Feb. 2012.

[6] C. R. Sullivan, B. A. Reese, A. L. F. Stein, and P. Aung Kyaw, "On Size and Magnetics: Why Small Efficient Power Inductors are Rare," in *Proc. of IEEE International Symposium on 3D Power Electronics Integration and Manufacturing (3D-PEIM)*, Raleigh, NC, USA, June 2016.

[7] J. W. Kolar, J. Biela, S. Waffler, T. Friedli, and U. Badstuebner, "Performance Trends and Limitations of Power Electronic Systems," in *Proc. of IEEE International Conference on Integrated Power Electronics Systems (CIPS)*, Nuremberg, Germany, Mar. 2010.

[8] D. Neumayr, D. Bortis, and J. W. Kolar, "The Essence of the Little Box Challenge - Part A: Key Design Challenges & Solutions," *in Proc. of CPSS Transactions on Power Electronics and Applications*, vol. 5, no. 2, pp. 158–179, 2020.

[9] C. P. Henze, H. C. Martin, and D. W. Parsley, "Zero-Voltage Switching in High Frequency Power Converter Using Pulse Width Modulation," in *Proc. of IEEE Applied Power Electronics Conference and Exposition (APEC)*, New Orleans, LA, USA, Feb. 1988.

[10] M. Kasper, R. Burkart, G. Deboy, and J. W. Kolar, "ZVS of Power MOS-FETs Revisited," *in Proc. of IEEE Transactions on Power Electronics*, vol. 31, no. 12, pp. 8063–8067, Dec. 2016.

[11] R. Joensson, "A New Switch Circuit for Frequency Inverters," in *Proc. of the International Conference on Power Electronics and Intelligent Motion (PCIM)*, Tokyo, Japan, December 1988.

[12] J. G. Cho, D. Y. Hu, and G. H. Cho, "Three-Phase Sine-Wave Voltage Source Inverter Using the Soft Switched Resonant Poles," in *Proc. of IEEE Industrial Electronics Society Conference*, Philadelphia, PA, USA, Nov. 1989.

[13] N. He, M. Chen, J. Wu, N. Zhu, and D. Xu, "20-kW Zero-Voltage-Switching SiC-MOSFET Grid Inverter with 300 kHz Switching Frequency," *in Proc. of IEEE Transactions on Power Electronics*, vol. 34, no. 6, pp. 5175 – 5190, June 2019.

[14] C. Marxgut, J. Biela, and J. W. Kolar, "Interleaved Triangular Current Mode (TCM) Resonant Transition, Single-Phase PFC Rectifier with High Efficiency and High Power Density," in *Proc. of IEEE International Power Electronics Conference (ECCE Asia)*, Sapporo, Japan, June 2010.

[15] D. Leuenberger and J. Biela, "Comparison of a Soft Switched TCM T-Type Inverter to Hard Switched Inverters for a 3-Phase PV Grid Interface," in *Proc. of the International Power Electronics and Motion Control Conference (EPE/PEMC)*, Novi Sad, Serbia, Sept. 2012.

[16] N. Haryani, S. J. Ohn, J. Hu, P. Rankin, R. Burgos, and D. Boroyevich, "A Novel ZVS Turn-on Triangular Current Mode Control with Phase Synchronization for Three Level Inverters," in *Proc. of IEEE Energy Conversion Congress and Exposition (ECCE USA)*, Portland, OR, USA, Sept. 2018.

[17] N. Haryani, B. Sun, and R. Burgos, "A Novel Soft Switching ZVS, Sinusoidal Input Boundary Current Mode Control of 6-Switch Three-Phase 2-Level Boost Rectifier for Active and Active + Reactive Power Generation," in *Proc. of IEEE Applied Power Electronics Conference and Exposition (APEC)*, San Antonio, TX, USA, March 2018.

[18] N. Haryani, B. Sun, and R. Burgos, "ZVS Turn-on Triangular Current Mode (TCM) Control for Three-Phase 2-Level Inverters with Reactive Power Control," in *Proc. of IEEE Energy Conversion Congress and Exposition (ECCE USA)*, Portland, OR, USA, Sept. 2018.

[19] Z. Huang, Z. Liu, F. C. Lee, and Q. Li, "Critical-Mode-Based Soft-Switching Modulation for High-Frequency Three-Phase Bidirectional AC-DC Converters," in *Proc. of IEEE Transactions on Power Electronics*, vol. 34, no. 4, pp. 3888–3898, April 2019.

[20] S. J. Ohn, N. Haryani, R. Burgos, and D. Boroyevich, "A Simplified Digital Closed-Loop Current Control of Three-Phase PV Inverter Operating in Triangular Conduction Mode," in *Proc. of IEEE International Power Electronics Conference (ECCE Asia)*, Busan, South Korea, May 2019.

[21] M. Antivachis, P. Niklaus, D. Bortis, and J. W. Kolar, "Input / Output EMI Filter Design for Three-Phase Ultra-High Speed Motor Drive GaN Inverter Stage," *accepted for publication in Proc. of CPSS Transactions on Power Electronics and Applications*, 2020.

[22] R. Joensson and I. Joensson, "PWM is Obsolete Technology from the '70s," in *Proc. of the International Conference on Power Electronics and Intelligent Motion (PCIM)*, Nuremberg, Germany, May 2009.

[23] B. Fan, Q. Wang, R. Burgos, A. Ismail, and D. Boroyevich, "Adaptive Hysteresis Current Based ZVS Modulation and Voltage Gain Compensation for High-Frequency Three-Phase Converters," *in Proc. of IEEE Transactions on Power Electronics*, vol. 36, no. 1, pp. 1143–1156, Jan. 2020.

[24] S. Zhang, G. Lan, Z. Dong, and X. Wu, "A High Efficiency Two-Stage ZVS AC/DC Converter with All SiC MOSFET," in *Proc. of IEEE International Power Electronics Conference (ECCE Asia)*, Kaohsiung, Taiwan, June 2017.

[25] Z. Huang, Z. Liu, F. C. Lee, Q. Li, and F. Xiao, "Critical-Mode-Based Soft-Switching Modulation for Three-Phase Inverters," in *Proc. of IEEE Energy Conversion Congress and Exposition (ECCE USA)*, Cincinnati, OH, USA, Oct. 2017.

[26] Z. Huang, Z. Liu, F. C. Lee, Q. Li, and F. Xiao, "Critical-Mode-Based Soft-Switching Modulation for Three-Phase Rectifiers," in *Proc. of IEEE Applied Power Electronics Conference and Exposition (APEC)*, San Antonio, TX, USA, March 2018.

[27] Z. Huang, Q. Li, and F. C. Lee, "Improved Three-Phase Critical-Mode-Based Soft-Switching Modulation Technique with Low Leakage Current for PV Inverter Application," in *Proc. of IEEE Energy Conversion Congress and Exposition (ECCE USA)*, Baltimore, MD, USA, Oct. 2019.

[28] J. Chen, D. Sha, J. Zhang, and X. Liao, "An SiC MOSFET Based Three-Phase ZVS Inverter Employing Variable Switching Frequency Space Vector PWM Control," *in Proc. of IEEE Transactions on Power Electronics*, vol. 34, no. 7, pp. 6320–6331, July 2019.

[29] A. Amirahmadi, H. Hu, A. Grishina, F. Chen, J. Shen, and I. Batarseh, "Hybrid Control of BCM Soft-Switching Three-Phase Micro-Inverter," in *Proc. of IEEE Energy Conversion Congress and Exposition (ECCE USA)*, Raleigh, NC, USA, Sept. 2012.

[30] A. Amirahmadi, H. Hu, A. Grishina, Q. Zhang, L. Chen, U. Somani, and I. Batarseh, "Hybrid ZVS BCM Current Controlled Three-Phase Microinverter," *in Proc. of IEEE Transactions on Power Electronics*, vol. 29, no. 4, pp. 2124–2134, April 2014.

[31] D. Zhang, M. Guacci, M. Haider, D. Bortis, J. W. Kolar, and J. Everts, "Three-Phase Bidirectional Buck-Boost Current DC-Link EV Battery Charger Featuring a Wide Output Voltage Range of 200 to 1000V," in *Proc. of IEEE Energy Conversion Congress and Exposition (ECCE USA)*, Detroit, MI, USA, Oct. 2020.

[32] M. Guacci, J. Azurza Anderson, K. L. Pally, D. Bortis, J. W. Kolar, M. Kasper, J. Sanchez, and G. Deboy, "Experimental Characterization of Silicon and Gallium Nitride 200V Power Semiconductors for Modular/Multi-Level Converters Using Advanced Measurement Techniques," *in Proc. of IEEE Journal of Emerging and Selected Topics in Power Electronics*, vol. 8, no. 3, pp. 2238–2254, Sept. 2020.

[33] P. Papamanolis, T. Guillod, F. Krismer, and J. W. Kolar, "Minimum Loss Operation and Optimal Design of High-Frequency Inductors for Defined Core and Litz Wire," *IEEE Open Journal of Power Electronics*, vol. 1, pp. 469–487, Sept. 2020.

[34] A. M. Hava, R. J. Kerkman, and T. A. Lipo, "A High-Performance Generalized Discontinuous PWM Algorithm," *in Proc. of IEEE Transactions on Industry Applications*, vol. 34, no. 5, pp. 1059–1071, Sept. 1998.

[35] L. Schrittwieser, J. W. Kolar, and T. B. Soeiro, "99% Efficient Three-Phase Buck-Type SiC MOSFET PFC Rectifier Minimizing Life Cycle Cost in DC Data Center," *in Proc. of CPSS Transactions on Power Electronics and Applications*, vol. 2, no. 1, pp. 47–58, July 2017.

[36] N. Haryani, "Zero Voltage Switching (ZVS) Turn-On Triangular Current Mode (TCM) Control for AC/DC and DC/AC Converters," Ph.D. dissertation, Virginia Polytechnic Institute and State University, 2019.

[37] J. W. Kolar, H. Ertl, and F. C. Zach, "Minimization of the Harmonic RMS Content of the Mains Current of a PWM Converter System Based on the Solution of an Extreme Value Problem," in *Proc. of the International Conference on on Harmonics in Power Systems*, Budapest, Hungary, Oct. 1990.

Michael Haider (S'17) received the M.Sc. degree in electrical engineering from the Swiss Federal Institute of Technology (ETH Zurich), Zurich, Switzerland, in 2017. He is currently working toward the Ph.D. degree at the Power Electronic Systems Laboratory, ETH, focusing on single-to-three phase converter systems, power pulsation buffer concepts and electrical machines. His further research interests include wide bandgap semiconductor device application and their integration into drive systems.

Jon Azurza Anderson (S'16) received his B.Sc. degree in Industrial Technology Engineering from TECNUN School of Engineering of the University of Navarra in 2014, his M.Sc. degree in Electrical Engineering from ETH Zurich (with distinction) in 2016, and his Ph.D degree in Power Electronics from ETH Zurich in 2020. In 2013 and 2014 he worked for Fraunhofer IIS in Nuremberg, Germany, developing software in the RFID & Radio Systems group. Since November 2016 he is with the Power Electronics Systems Laboratory (PES) at ETH Zurich as a scientific assistant, focusing on ultra-high efficiency three-phase multi-level PWM converters.

Spasoje Mirić (S'13) received the B.Sc. and M.Sc. degrees in electrical engineering in 2012 and 2013, respectively, from the University of Belgrade, Belgrade, Serbia. He is currently working towards his Ph.D. degree in electrical engineering at the Swiss Federal Institute of Technology (ETH) Zurich, Zurich, Switzerland. His research interests are novel electrical machine topologies, linear machines and bearingless motors for highly dynamic actuator systems.

Neha Nain received the B.E. degree in Electrical and Electronics Engineering from P.E.S Institute of Technology, Bangalore, India in 2015, and the M.Sc. degree in Electrical Engineering and Information Technology from the Swiss Federal Institute of Technology (ETH), Zurich, Switzerland in 2020. From July 2015 – August 2018, she was with Texas Instruments working as Systems Engineer. In November 2020, she joined the Power Electronic Systems Laboratory (PES), ETH Zurich as a Ph.D. student, focusing on compact, high-efficiency DC/AC and AC/AC power converters based on wide band-gap power semiconductors.

Grayson Zulauf (S'16) received the B.A. degree in engineering sciences in 2012 and the B.E. degree in electrical engineering with highest honors from the Thayer School of Engineering, Dartmouth College, Hanover, NH, USA, in 2013, and the M.S. degree in electrical engineering from Stanford University, Stanford, CA, USA, in 2018. From 2013 to 2016, he was an Electrical Engineer and Product Manager at Motiv Power Systems. In 2019, he was an Academic Guest in the Power Electronics Systems Laboratory at ETH Zurich as a ThinkSwiss Research Fellow. In 2020, he received the Ph.D. degree in electrical engineering from Stanford University, Stanford, CA, USA. He is currently an Activate / Cyclotron Road Fellow at Berkeley National Lab.

Johann W. Kolar (F'10) received his M.Sc. degree in Industrial Electronics and Control Engineering and his Ph.D. degree in Electrical Engineering (summa cum laude/promotio sub auspiciis praesidentis rei publicae) from the Vienna University of Technology, Austria, in 1997 and 1999, respectively. Since 1984, he has been working as independent researcher and international consultant in close collaboration with the Vienna University of Technology, in the fields of power electronics, industrial electronics and high performance drive systems. He is currently a Full Professor and the Head of the Power Electronic Systems Laboratory at the Swiss Federal Institute of Technology (ETH) Zurich. He has proposed numerous novel PWM converter topologies, modulation and control concepts, multi-objective power electronics design procedures, etc. and has supervised 75+ Ph.D. students. He has published 900+ scientific papers in international journals and conference proceedings, 4 book chapters, and has filed 190+ patents. He has presented 30+ educational seminars at leading international conferences, has served as IEEE PELS Distinguished Lecturer from 2012 through 2016, and has received 36 IEEE Transactions and Conference Prize Paper Awards, the 2014 IEEE Power Electronics Society R. David Middlebrook Achievement Award, the 2016 IEEE William E. Newell Power Electronics Award, the 2016 IEEE PEMC Council Award, and two ETH Zurich Golden Owl Awards for excellence in teaching. He has initiated and/or is the founder of 4 ETH Spin-off companies. The focus of his current research is on ultra-compact and ultra-efficient SiC and GaN converter systems, ANN-based power electronics components and systems design, Solid-State Transformers, Power Supplies on Chip, as well as ultra-high speed and ultra-light weight drives, bearingless motors, and energy harvesting.

Dehong Xu (Fellow, IEEE) was born in China, in 1961. He received the B.S., M.S., and Ph.D. degrees from the Department of Electrical Engineering, Zhejiang University, Hangzhou, China, in 1983, 1986, and 1989, respectively. Since 1996, he has been with the College of Electrical Engineering, Zhejiang University, China, as a Full Professor. From June 1995 to May 1996, he was a Visiting Scholar with the University of Tokyo, Tokyo, Japan. From June to December 2000, he was a Visiting Professor with CPES of Virginia Tech, Blacksburg, VA, USA. He has authored or coauthored six books and more than 200 IEEE Journal or Conference papers. He owns more than 30 Chinese patents and three U.S. patents. From February to April 2006, he was a Visiting Professor with ETH, Zürich, Switzerland. His current research interests include power electronics topology and control, power conversion for energy saving, and renewable energy. Dr. Xu is the recipient of four IEEE journal or conference paper awards. In 2016, he was the recipient of the IEEE PELS R. D. Middlebrook Achievement Award. Since 2013, he has been the President of the China Power Supply Society. He is an At-Large Adcom Member of the IEEE Power Electronics Society from 2017 to 2019. He is an Associate Editor of the IEEE TRANSACTIONS ON POWER ELECTRONICS. He was the IEEE PELS Distinguish Lecturer from 2015 to 2018.

Gerald Deboy (SM'98) received the M.Sc. and Ph.D. degree in physics from the Technical University Munich in 1991 and 1996 respectively. He joined Infineon Technologies AG in 1994 and is currently heading a group looking into opportunities and requirements for emerging applications. He has authored and coauthored more than 70 papers in national and international journals including contributions to three student text books. He holds more than 60 granted international patents and has more applications pending.